

Supporting information for: Dynamic of optically directed assembly/disassembly of gold nanoplatelet arrays

Delphine Coursault,[†] Nishant Sule,[†] John Parker,^{†,‡} Ying Bao,^{†,¶} and Norbert F.
Scherer^{*,†,¶}

[†]*James Franck Institute, University of Chicago, IL 60637, USA*

[‡]*Department of Physics, University of Chicago, IL 60637, USA*

[¶]*Department of Chemistry, University of Chicago, IL 60637, USA*

E-mail: nfschere@uchicago.edu

Experimental

Au nanoplatelet synthesis and properties

The Au nanoplatelets were synthesized via a reported method.^{S1} In a typical synthesis, a solution was first prepared by mixing 0.143 mM NaNO₃, 0.143 mM KI, 0.477 mM HAuCl₄ and 19.1 mM PVP to a total volume 209.6 mL (diluted with water). Then, 0.2 mL of 1 M NaOH was added into the mixture in order to increase the pH. This solution was left undisturbed for 18 h. The final products, including Au NPLs and Au nanospheres, were collected and prepared for further use after decanting the supernatant and redispersing the pellet in deionized water. The Au nanoplatelet/Au colloid suspension was drop-cast onto

a silicon substrate for structural characterization by scanning electron microscopy (SEM; Figure 2 in the main text). The average diameter of the NPLs is about 700nm with a thickness of 25 nm (aspect ratio=28).

Optical trapping setup

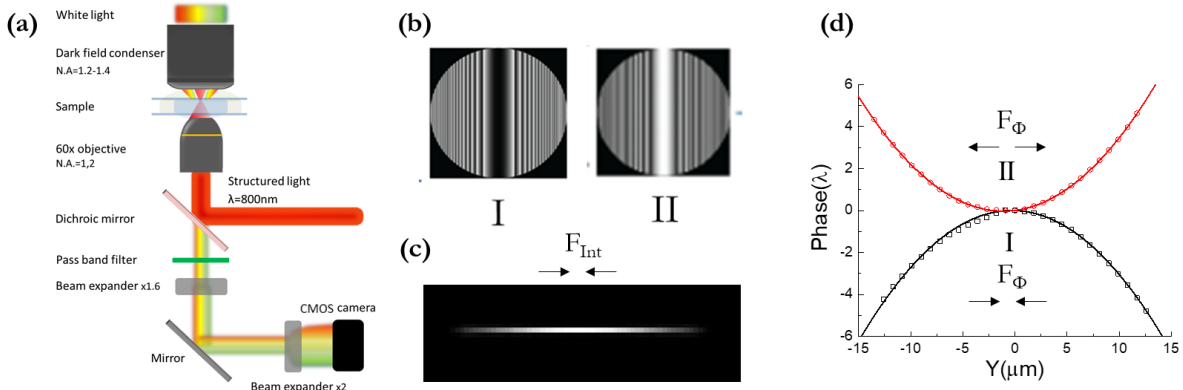


Figure S1: Optical trapping and dark-field microscopy system, phase masks and measured phase profiles of optical line trapping beams. (a) Optical trapping setup (b) Cylindrical lens phase masks on the SLM; convex (type I) and concave (type II) phase masks (top) to create an optical line. (c) Line intensity profile calculated (by FFT of the phase mask) with a Gaussian intensity profile and (d) phase distribution along the line trap as measured with a wavefront sensor. Note the measured values are in excellent agreement with an ideal parabolic phase function (fits).

The experiments described in the main text, were performed in an optical trapping and microscopy setup described in [2]. A schematic of the setup is presented in Figure S1a. The phase masks I and II in Figure S1b allow shaping the phase structure of the Gaussian beam that is focused into optical line beams corresponding to the type I and type II traps in the main text. Both shaped beams have the same Gaussian intensity profile (Figure S1c) inducing the same attractive force towards the center of the line trap, but with opposite phase gradients ($\pm 0.58\lambda/\mu\text{m}$, λ is the wavelength of the incident light) as shown by the phase profiles (Figure S1d). The phase was measured with a Shack-Hartmann wavefront sensor (Thorlabs WFS150-5C).

Images of the focused beams (line trap and zero-order beams, Figure S2) were taken by

retro-reflecting the focused beam with a gold mirror and recorded with a sCMOS (Andor NEO) camera. The beam intensity is actually smooth inside the sample. The images are distorted by interference with the light reflected from both surfaces of the dichroic mirror toward the detector. The beam intensity is actually smooth inside the sample.^{S3}The same sCMOS camera was used to record dark-field microscopy Videos of the trapped particles at a rate of 65fps.

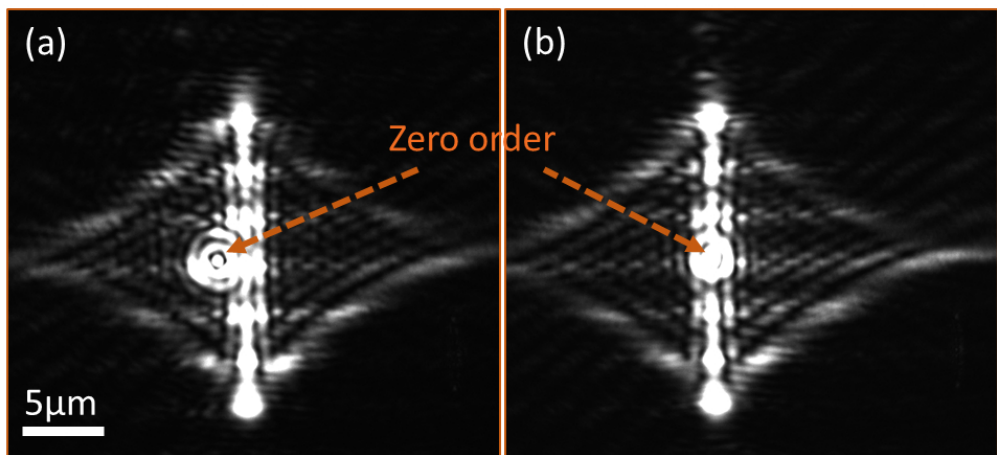


Figure S2: Microscopy images of the beams described in Figure S1 when reflected from a gold mirror positioned at the focal (trapping) plane of the optical microscope. The beam is shaped by the SLM into a line trap. The intense Gaussian spot corresponds to the zero-order beam, which is approximately 5% of the total optical power. Adjusting a Zernicke coefficient for “tilt” allows shifting (a) or superimposing (b) the line trap to the zero-order.

NPL motion

The NPLs were tracked manually using the plug-in “manual track” from ImageJ because automated tracking failed to detect all the particles in a frame and to link them into trajectories due to both the non-Gaussian distribution of the light scattered by the NPLs (the scattering comes mainly from the NPL edges) and insufficient contrast. Indeed the light scattered by the NPL is maximum at wavelengths longer than 700nm (Figure 2 in the main text), but our setup uses a short pass filter to cut off all the scattered light with wavelengths longer than 750nm.

We switched the light polarization of the incident beam from linear to an elliptical (ideally circular) polarization by applying a step function waveform with a 5 second periodicity to a liquid crystal retarder device. The NPLs can be made to rotate by elliptically polarized light, as evidenced by the the continuous change in brightness and contrast of the light scattered by the NPLs (see video “rot”). Snapshots and a schematic of the orientation of the NPLs is shown in Figure S3.

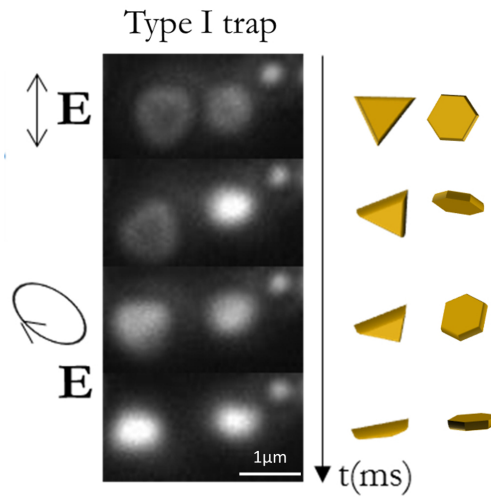


Figure S3: NPL rotation induced by elliptically polarized light. Consecutive frames in a Video of dark-field images of rotating NPLs. The 3D rotation occurs when switching from linear to elliptical polarization. The frame rate is 65 frames per second.

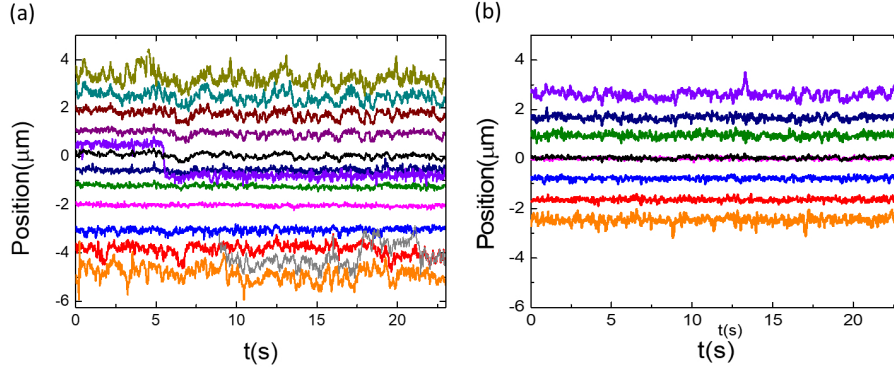


Figure S4: NPL trajectories in a line trap at steady-state. Trajectories of the single NPLs in an array formed in the presence of the zero-order beam: (a) when the polarisation is parallel to the axis of the line trap; (b) when the polarisation is perpendicular to the axis of the line trap. For both, the pink trajectory is that of the NPL trapped at the location where the zero-order beam is superimposed to the optical line. The black trajectory represents the mean trajectory of the array. Note that the position fluctuations of the NPLs increase away from the center of the line trap, which reflects both the decreasing intensity of the optical trap and the reduced interaction with the neighboring NPLs (i.e. fewer neighbors).

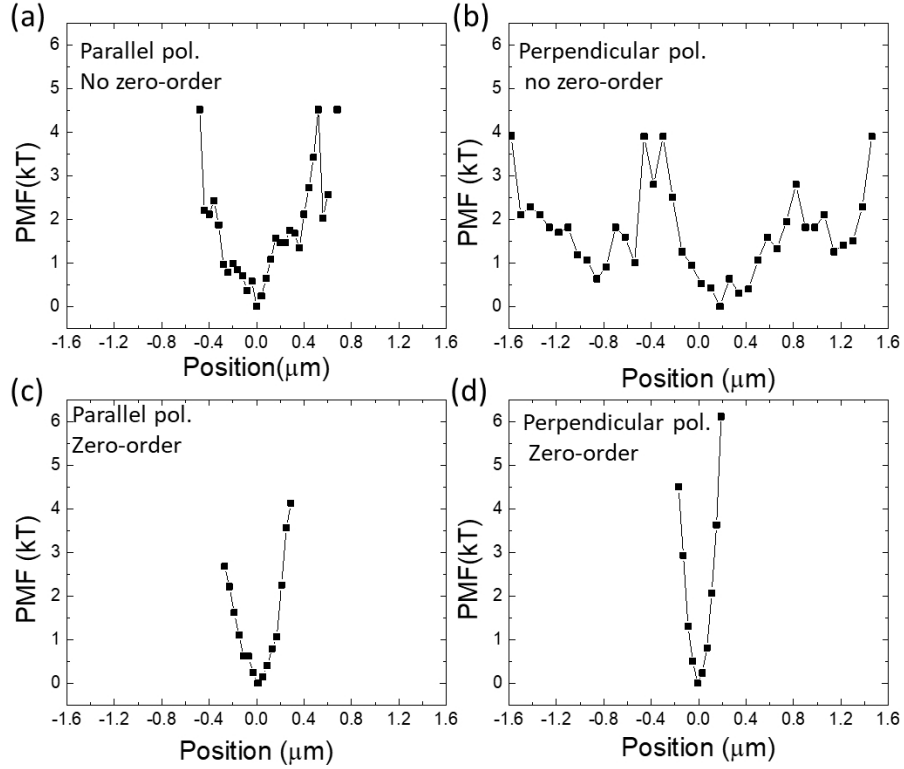


Figure S5: Potential of mean force (PMF) of NPLs at steady-state. PMF of the mean trajectory calculated for the linear NPL arrays presented in Figure 3 and Figure S4 for light polarizations (a) parallel and (b) perpendicular to the optical line in the absence of the zero-order beam, in the presence of the zero-order beam when the polarisation is (c) and perpendicular (d) parallel to the axis of the line trap. The PMF are narrower in the presence of the zero-order beam. The zero-order beam has a stronger stabilizing effect than the number of NPL. Indeed, despite a smaller number of NPLs in the array, the PMF of the mean trajectory is 2 times narrower than in absence of the zero-order beam.

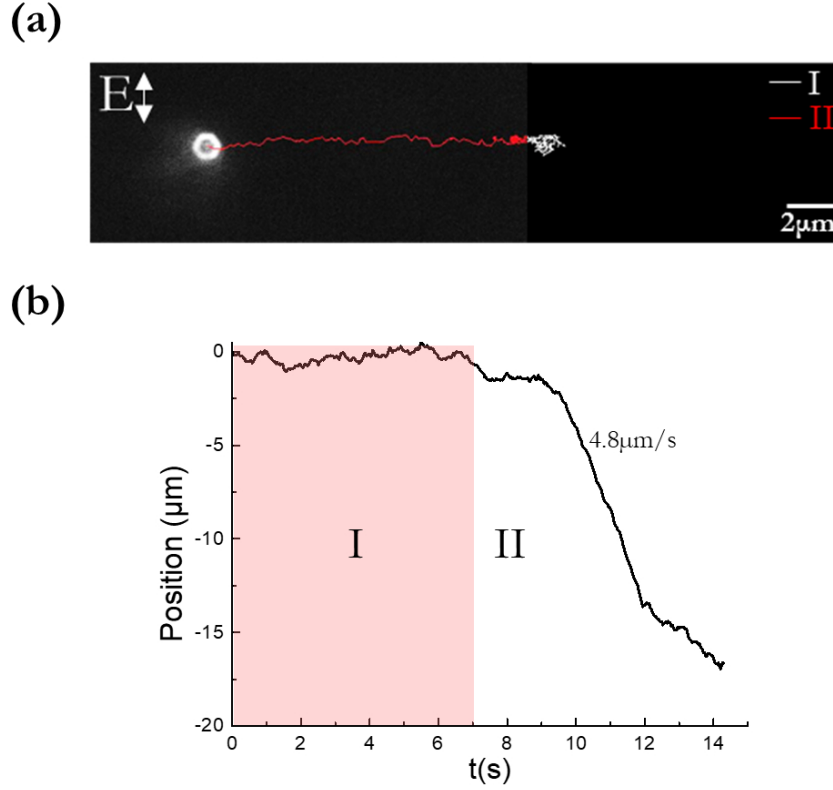


Figure S6: Single NPL driven motion. We trapped a single NPL in an optical line (type I trap) at steady state, then changed the phase to type II at 7sec. (a) Dark-field image of a single NPL with its overlaid trajectory (red). (b) Trajectory of NPL along the optical line axis at steady state in a type I trap and then driven in a type II trap. The NPL escapes the trap center after a couple of seconds (lag) and then drifts at constant speed ($4.8 \mu\text{m/s}$) until the lateral confinement is too weak (beginning at about 12 sec) to maintain the linear motion. There is no evidence for any step-like or discontinuity features in the single NPL trajectory during the drift. This observation is to be viewed in contrast to the very step like motion in the case of multiple NPLs being driven out of or being driven into the line trap as in Figure 4 of the main text.

Influence of the viscous drag on NPL motion

The temperature increase of the Au NPL is calculated according to:^{S4}

$$\Delta T = \frac{\sigma_{abs} I}{4\pi\kappa_s \beta R_{eq}} \quad (1)$$

$$(2)$$

with $\sigma_{abs} = 0.058\mu\text{m}^2$ at $\lambda = 800$ nm. Since only 80% of the intensity is transmitted by the objective, $I = \frac{P}{\pi\sigma_x\sigma_y} = 3.1\text{mW}.\mu\text{m}^{-2}$.^{S2,S5} κ_s is the conductivity of the surrounding medium, $\kappa_s=0.6$ W.m⁻¹.K⁻¹, β is a dimensionless geometrical correction coefficient and is equal to 1.7884 according to [S6], and $R_{eq} = (\frac{3D^2d}{16})^{\frac{1}{3}} = 0.132$ μm . The calculated increase is 100°C. Due to the large surface area of the NPL and the short distance to the glass we expect the temperature to be reduced by a factor 6. S6 We estimated that the inward fluid (parallel to the glass) flow would be of about 4nm/s for a temperature of 40°. S7 The induced flow should not affect the NPL dynamics.

We calculated the translational drag coefficient for a NPL oriented with its short axis perpendicular to the motion to determine whether hydrodynamic drag forces may be responsible for the slower motion of the NPLs. According to Perrin's formula,^{S8} the friction coefficient for an oblate ellipsoid is:

$$\gamma_o = 32\pi\eta \frac{a^2 - b^2}{(2a^2 - 3b^2)S - 2a} \text{ with } a < b(= c), \quad (3)$$

where

$$S = \frac{2}{\sqrt{b^2 - a^2}} \arctan \frac{\sqrt{b^2 - a^2}}{a} \quad (4)$$

For a disk of height a=12.5 nm and a radius b=350 nm immersed in water ($\eta_{H_2O}=0,66.10^{-3}$ Pa.s at 40°C) $\gamma_o^{NPL} = 0.44 \times 10^{-12}$ (N.s)/m vs $\gamma_o^{NP} = 1.32 \times 10^{-9}$ (N.s)/m for a 200nm diameter nanosphere. Thus, assuming equal electrodynamic forces, the hydrodynamics suggest that a nanosphere would move slower than a NPL by 10³ times. A correction that takes into account the distance to the substrate would decrease the sphere drag by one order of magnitude. Figure S7 show the correction in the near wall regime that changes very little in the range $r \ll H$ from the more extreme lubrication regime.

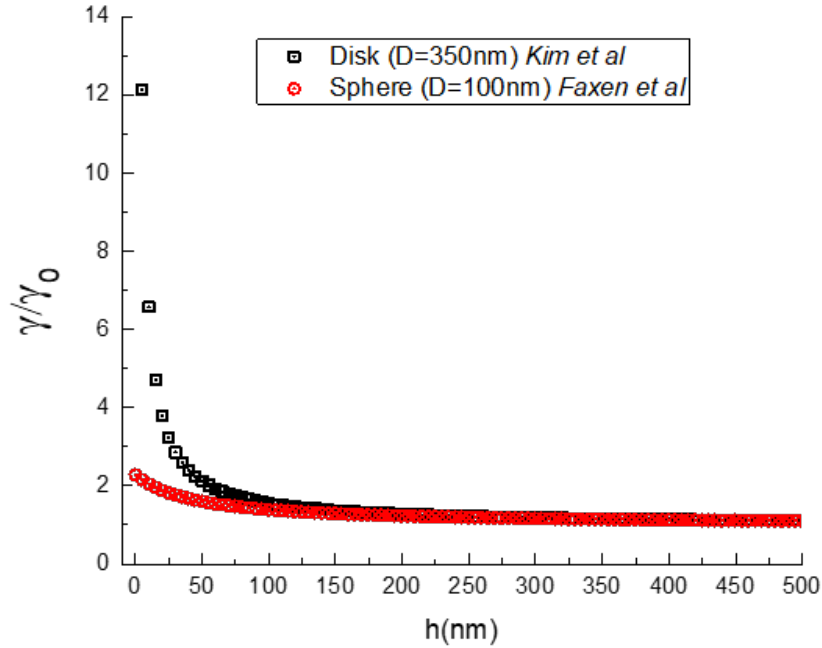


Figure S7: Calculated viscous drag coefficient correction for a 100nm radius sphere and a disk of 350nm radius as a function of the distance to the substrate. The results follow from [S9] for a sphere and [S10] for the disk.

Simulations

Multipolar analysis of the scattered fields

To perform the multipolar FDTD simulations, we use the freely available software package MEEP^{S11} combined with a multipolar analysis technique to identify the modes of the Au nanoplatelet.^{S12} A plane wave pulse is propagated towards the nanoplatelet in a water medium ($n=1.33$), and the fields are Fourier transformed over a range of wavelengths from 500 nm to 1500 nm. The electric field enhancement, $E_{\text{enh}} = |\mathbf{E}_{\text{tot}}(\omega)|/|\mathbf{E}_{\text{inc}}(\omega)|$, is then obtained in XY and XZ cross-sections of the nanoplatelet. Figure 2(a,b) of the main text shows the electric field intensity corresponding to a wavelength of the incident beam $\lambda = 800$ nm. Figure S8 shows additional results obtained for a wavelength of the incident beam

$\lambda = 742$ nm and $\lambda = 1200$ nm for which the octupole and the dipole respectively dominate as shown in Figure 2c of the main text. At shorter wavelengths, the electric field becomes more complex and has a greater field enhancement due to higher order plasmon modes (see extinction spectra in Figure 2c).

The multipole expansion technique has been detailed in other work,^{S12} so only a summary is presented here. First, a Near-to-Far-Field (NTFF) transformation of the electromagnetic fields is performed to obtain the Fourier transformed fields on the surface of a far-field spherical monitor centered on the nanoplatelet. The scattered electric field, $\mathbf{E}_{\text{scat}}(\omega, r, \theta, \phi)$, is then expanded into the vector spherical harmonics (VSHs)^{S13,S14}

$$\mathbf{E}_{\text{scat}}(\omega, r, \theta, \phi) = \sum_{l=1}^{\infty} \sum_{m=-l}^{m=l} a_{lm}(\omega) \mathbf{N}_{lm} + b_{lm}(\omega) \mathbf{M}_{lm} \quad (5)$$

where $a_{lm}(\omega)$ and $b_{lm}(\omega)$ are the complex multipolar coefficients corresponding to the electric (\mathbf{N}_{lm}) and magnetic (\mathbf{M}_{lm}) modes, respectively, of order l and orientation m .

An integral expression for the the multipolar coefficients $a_{lm}(\omega)$ and $b_{lm}(\omega)$ can be determined by exploiting the orthogonality of the VSHs

$$\begin{aligned} a_{lm}(\omega) &= \oint_{\Omega} \mathbf{E}_{\text{scat}}(\omega, r = r_0, \theta, \phi) \cdot \mathbf{N}_{lm}(\omega, r = r_0, \theta, \phi) d\Omega \\ b_{lm}(\omega) &= \oint_{\Omega} \mathbf{E}_{\text{scat}}(\omega, r = r_0, \theta, \phi) \cdot \mathbf{M}_{lm}(\omega, r = r_0, \theta, \phi) d\Omega \end{aligned} \quad (6)$$

where r_0 is the radius of the spherical monitor and Ω is the entire sphere surface. Eq.(6) is used to numerically compute the multipolar scattering coefficients at each frequency ω of interest. Finally, we use a relation between the multipolar scattering coefficients and the scattering cross-section^{S13}

$$\sigma_{\text{scat}}(\omega) = k^2 \sum_{l=1}^{\infty} \sum_{m=-n}^n l(l+1) (|a_{lm}(\omega)|^2 + |b_{lm}(\omega)|^2) \quad (7)$$

where $k = 2\pi n_b/\lambda$, and $n_b = 1.33$. Each l term in the sum provides the scattering cross-

section of the corresponding multipolar mode, where $l = 1$ is dipole, $l = 2$ is quadrupole, etc. These multipolar cross-sections are shown in Figure 2(c) of the main text. Total scattering and absorption cross-sections are obtained through traditional FDTD techniques.

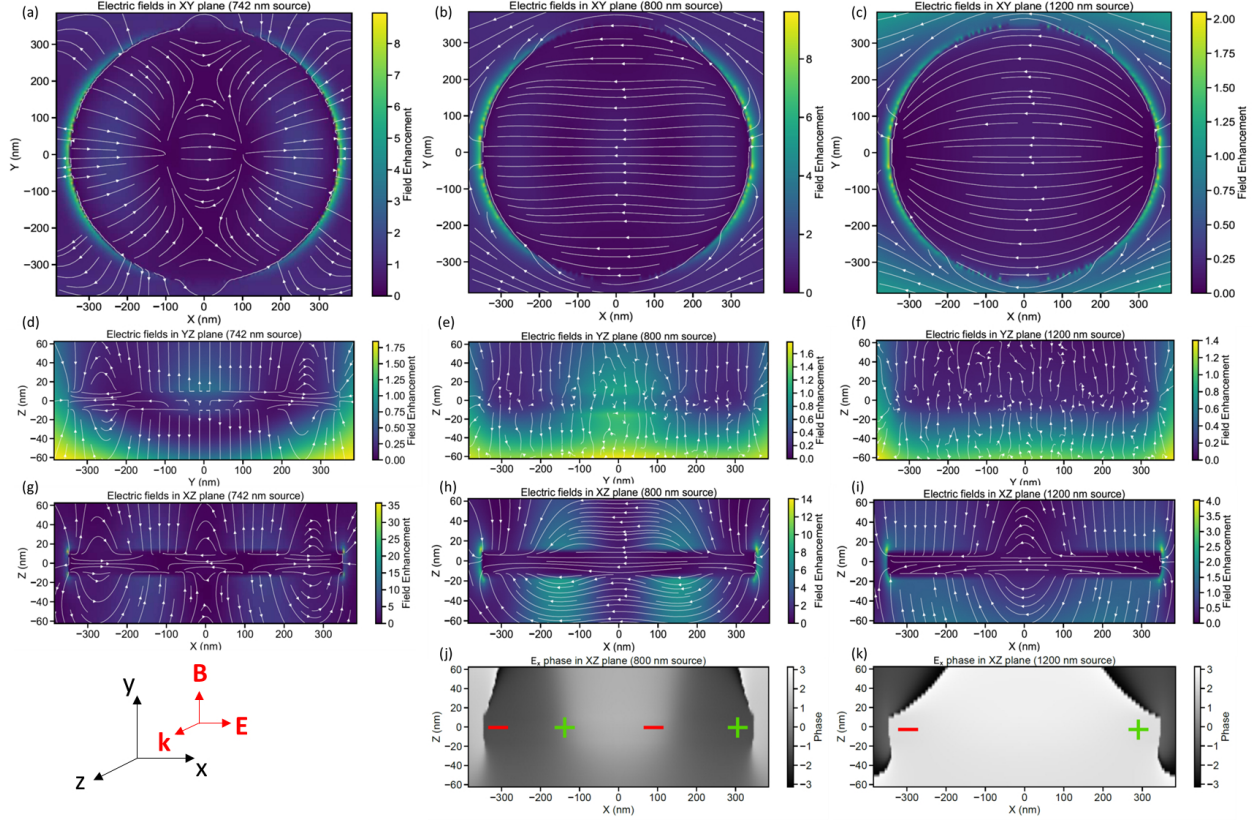


Figure S8: FDTD simulations of a Au NPL (disk of 700 nm diameter and 25 nm height) in $n=1.33$ for water: (a,b) Map of the electric field enhancement at $\lambda=742\text{nm}$ (a,d,g), 800nm (b,e,h), 1200nm (c,f,i)(vacuum) for incident light propagating along the z direction and polarized along the x axis (a,b,c) in the XY plane, parallel to the plate (d,e,f) in the YZ plane perpendicular to the NPL, (g,h,i) in the XZ plane perpendicular to the NPL. Phase Map of the electric field at $\lambda=800\text{nm}$ (j), 1200nm (k) in the XZ plane perpendicular to the NPL.

NPL motion in optical line traps by combined electrodynamics-Langevin dynamics simulations

The results of finite difference time domain (FDTD) simulations shown in Figure 2e–f were performed using an in-house 3D FDTD code where the grid cell size in the plane and along the thickness of the nanoplatelet was different. The asymmetric grid cells allowed simulating

the high aspect ratio particles. We assumed the nanoplatelet to be 700 nm in diameter and 25 nm in thickness. The optical line trap was introduced in the simulation using the scattered-field technique^{S15,S16} in which the incident electric field was described as

$$E(x, y, z, t) = E_{0l} e^{-\frac{(x-x_0)^2}{2x_w^2}} e^{-\frac{(y-y_0)^2}{2y_w^2}} e^{i(kz-\omega t)} e^{\pm ik_l(y-y_0)^2} + E_{0z} e^{-\frac{(x-x_0)^2}{2x_w^2}} e^{-\frac{(y-y_0)^2}{2x_w^2}} e^{i(kz-\omega t)} \quad (8)$$

This equation represents an asymmetric Gaussian beam that is propagating along the z direction. Here, $E_{0l} = \sqrt{2I_{0l}/c\epsilon_0 n}$ is the electric field magnitude, I_{0l} is the intensity of the line trap, and $n = 1.33$ is the refractive index of water. The constants, $x_w=450$ nm and $y_w=35$ μ m define the full-width half-max (FWHM) along the x and y directions. The wave vector and angular frequency of the beam are, $k = 2\pi n/\lambda$, and $\omega = kc/n$, respectively, where, λ is the free-space wavelength and c is the free-space speed of light. The parabolic phase profile of the beam along the y direction is quantified using the constant, $k_l = 9 \times 10^{10}$ m⁻². The sign of k_l determines the direction of the optical force that depends on the phase gradient, with $+$ ($-$) resulting in outward-from-center (inward-to-center) forces. The center of the simulation domain is given by x_0 and y_0 . The zero-order beam was simulated by adding a symmetric Gaussian beam to the line trap (second term on the right hand side in Eq. 8) where, the magnitude of the zero-order electric field is given by $E_{0z} = \sqrt{2I_{0z}/c\epsilon_0 n}$. The incident magnetic field was calculated from Ampere's law for each time step before updating the scattered fields in the main FDTD calculation.

The electrodynamic forces on the Au nanoplatelets as a function of position along the trap were calculated by placing one particle in the center of the domain and moving a second particle along the y direction. Then, at each position along y , the incident beam was propagated for 10 to 15 cycles and the forces were computed using the Maxwell Stress Tensor. The Drude model was used to describe the dispersive Au nanoplatelets using the auxiliary differential equation method.^{S16} We used the following Drude parameters for Au: $\epsilon_\infty = 11.02$, $\omega_p = 2.33 \times 10^{15}$ s⁻¹, and $\gamma_p = 9.84 \times 10^{13}$ s⁻¹.

We simulated particle trajectories by coupling the electrodynamic forces to a Langevin equation of motion (ED-LD simulations).^{S17} In order to simplify the kinematics of the particles, we simulated only the in-plane motion, *i.e.*, using only the x and y components of the optical forces and assuming that all forces (including the random thermal forces in the Langevin equation) along the z direction were zero.

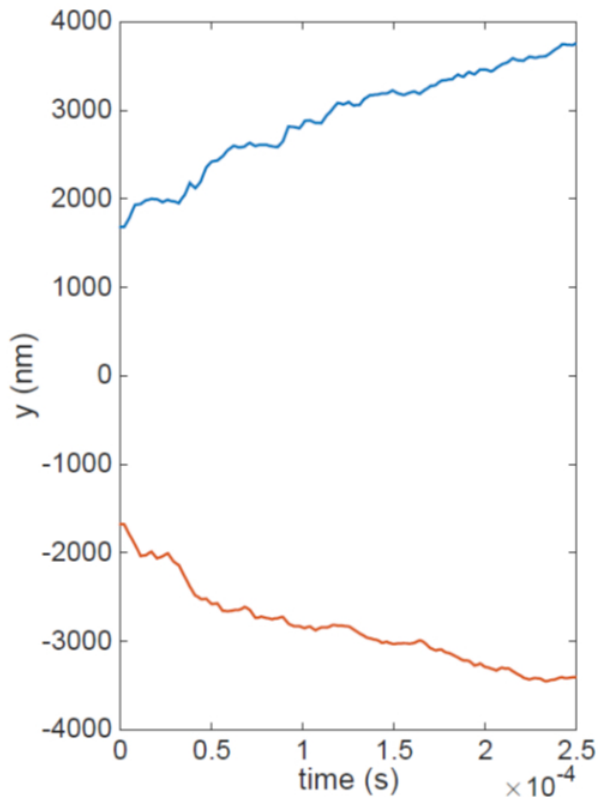


Figure S9: Simulated trajectories of the two outer NPL of a 5 NPLs linear array drifting in a type II trap. The step-like features in the trajectories resemble the steps on halting-plateaus observed in the experiments.

References

- (S1) Viarbitskaya, S.; Teulle, A.; Marty, R.; Sharma, J.; Girard, C.; Arbouet, A.; Dujardin, E. *Nature Materials* **2013**, *12*, 426–432.
- (S2) Yan, Z.; Sajjan, M.; Scherer, N. F. *Physical Review Letters* **2015**, *114*, 143901.

- (S3) Yan, Z.; Shah, R. A.; Chado, G.; Gray, S. K.; Pelton, M.; Scherer, N. F. *ACS Nano* **2013**, *7*, 1790–1802.
- (S4) Baffou, G.; Quidant, R. *Laser & Photonics Reviews* **2013**, *7*, 171–187.
- (S5) Demergis, V.; Florin, E.-L. *Nano Letters* **2012**, *12*, 5756–5760.
- (S6) Baffou, G.; Quidant, R.; Girard, C. *Phys. Rev. B* **2010**, *82*, 165424.
- (S7) Donner, J. S.; Baffou, G.; McCloskey, D.; Quidant, R. *ACS Nano* **2011**, *5*, 5457–5462.
- (S8) Perrin, Francis, *J. Phys. Radium* **1934**, *5*, 497–511.
- (S9) Ambari, A.; Gauthier-Manuel, B.; Guyon, E. *Journal of Fluid Mechanics* **1984**, *149*, 235–253.
- (S10) Kim, M.-U.; Kim, K. W.; Cho, Y.-H.; Kwak, B. M. *Fluid Dynamics Research* **2001**, *29*, 137.
- (S11) Ardavan, F. O.; David, R.; Mihai, I.; Peter, B.; Joannopoulos, J. D.; Steven, G. J. *Computer Physics Communications* **2010**, *181*, 687–702.
- (S12) Parker, J.; Gray, S.; Scherer, N. *ArXiv e-prints* **2017**, <http://adsabs.harvard.edu/abs/2017arXiv171106833P>.
- (S13) Mühlig, S.; Menzel, C.; Rockstuhl, C.; Lederer, F. *Metamaterials* **2011**, *5*, 64–73.
- (S14) Grahn, P.; Shevchenko, A.; Kaivola, M. *New Journal of Physics* **2012**, *14*, 093033.
- (S15) Sun, W.; Pan, S.; Jiang, Y. *Journal of Modern Optics* **2006**, *53*, 2691–2700.
- (S16) Kong, S. C.; Simpson, J. J.; Backman, V. *IEEE Microwave and Wireless Components Letters* **2008**, *18*, 4–6.
- (S17) Sule, N.; Rice, S. A.; Gray, S. K.; Scherer, N. F. *Optics Express* **2015**, *23*, 29978–29992.